

Lagrangian coherent structures and entrainment near the turbulent/non-turbulent interface of a gravity current

Marius M. Neamtu-Halic¹†, Dominik Krug², George Haller³ and Markus Holzner¹

¹Institute of Environmental Engineering, ETH Zurich, CH-8039 Zurich, Switzerland

²Physics of Fluids Group and Twente Max Planck Center, Department of Science and Technology, Mesa+ Institute, and J.M. Burgers Center for Fluid Dynamics, University of Twente, PO Box 217, 7500 AE Enschede, The Netherlands

³Institute of Mechanical Systems, ETH Zurich, 8092 Zurich, Switzerland

(Received xx; revised xx; accepted xx)

In this paper, we employ Lagrangian coherent structures (LCSs) theory for the three-dimensional vortex eduction and investigate the effect of large-scale vortical structures on the turbulent/non-turbulent interface (TNTI) and entrainment of a gravity current. The gravity current is realized experimentally and different levels of stratification are examined. For flow measurements, we use a multivolume three-dimensional particle tracking velocimetry technique. To identify vortical LCSs (VLCSs), a fully automated 3D extraction algorithm for multiple flow structures based on the so-called Lagrangian-Averaged Vorticity Deviation method is implemented. The size, the orientation and the shape of the VLCSs are analyzed and the results show that these characteristics depend only weakly on the strength of the stratification. Through conditional analysis, we provide evidence that VLCSs modulate the average TNTI height, affecting consequently the entrainment process. Furthermore, VLCSs influence the local entrainment velocity and organize the flow field on both the turbulent and non-turbulent sides of the gravity current boundary.

Key words: Stratified turbulence, gravity currents, Lagrangian coherent structures

1. Introduction

The flow in the vicinity of the sharp interface that is widely observed to form between a turbulent flow and non-turbulent surroundings, e.g. a chimney plume issuing into quiescent air, has received considerable attention in the literature over the last decades (e.g. Dimotakis 2000; Holzner *et al.* 2008; da Silva *et al.* 2014). Among others, the main motivation for these studies stems from the fact that across turbulent/non-turbulent interfaces (TNTIs), fluid is continuously incorporated into the turbulent flow, a process known as turbulent entrainment. The entrainment rate has direct bearing on mixing properties and global dynamics of the flow and is therefore of high relevance and interest in many applications, e.g. jet-, wake- and boundary layer-flows.

† Email address for correspondence: neamtu@ifu.baug.ethz.ch

To date, much research has focused on small-scale properties of the entrainment process (see e.g. Westerweel *et al.* 2005; Holzner & Lüthi 2011; Silva *et al.* 2018) and it is now well established (Mathew & Basu 2002; Westerweel *et al.* 2009), that the process by which non-turbulent fluid initially acquires vorticity is of viscous nature, as originally envisioned by Corrsin & Kistler (1955). However, the overall entrainment rate is known to be independent of viscosity or, in other terms, of the Reynolds number (see e.g. Tritton 1988; Tsinober 2009). It is therefore believed that structures at larger scales act to cancel the Reynolds number dependence of the small-scale process. That is to say that, even though locally non-turbulent fluid becomes turbulent via viscous diffusion of vorticity, the overall entrainment is imposed by fluid motion at larger scales which control the surface area of the TNTI (Townsend 1980; Sreenivasan *et al.* 1989). Recently, Lee *et al.* (2017) used conditional analysis to show that the TNTI surface area of a turbulent boundary layer increases in the vicinity of large-scale motions (LSMs). However, a similar observation is missing for other flows, far from the wall, and nowadays it is not clear how the fluid motion near the TNTI is related to the vortical structures in the flow.

da Silva & dos Reis (2011) visualized the vortical structures near the TNTI of a turbulent planar jet. They suggested that the large-scale vortices sitting on the TNTI are mostly defining its shape. Moreover, they conclude that the characteristic vorticity jump of the TNTI, as well as its thickness, is imposed by the radial vorticity distribution of these structures.

Nevertheless, progress in our understanding of the relation between the large-scale vortical structures and TNTI has been hampered by the arbitrariness in the vortex structure definition. Often structures are extracted based on arbitrary thresholds and based on quantities that are not invariant to a change of system of reference, i.e. they are not objective. Newly developed, Lagrangian methods (for a review, see Haller 2015) for vortex identification constitute a promising tool to overcome this issue.

Since the initial work of Haller & Yuan (2000), the Lagrangian coherent structures (LCSs) theory aims to identify vortical structures (referred hereinafter as VLCSs to distinguish them by other type of LCSs) using dynamical systems approaches, overcoming the arbitrariness that characterizes the classical non-objective methods, such as Q - (Hunt *et al.* 1988), Δ - (Chong *et al.* 1990) and λ_2 -*criterion* (Jeong & Hussain 1995). LCSs approaches are mostly based on stretching requirements (Haller 2015) and identify highly coherent, black-hole type material regions with high accuracy, but at substantial computational cost (see e.g. Haller & Beron-Vera 2013; Hadjighasem & Haller 2016).

Recently, a less computationally expensive approach has been developed that replaces the stretching-based coherence requirement with rotational coherence. This method uses a new dynamic version of the classic polar decomposition introduced in Haller (2016) and identifies the initial positions of VLCSs as tubular level surfaces of the so-called Lagrangian-Averaged Vorticity Deviation (LAVD). Haller *et al.* (2016) identified vortical structures, using LAVD-based methods, in two-dimensional and three-dimensional flow fields. However, as highlighted by Haller *et al.* (2016), a fully automated implementation of LAVD methods for multiple three-dimensional coherent structures is still missing.

In the present work, we seek to implement a three-dimensional VLCS extraction method based on the LAVD theory of Haller *et al.* (2016) and apply it to experimental data of a gravity current. The gravity current constitutes an interesting flow case for two reasons. On one hand, it has important practical applications, e.g. river plumes, katabatic winds and oceanic overflows. On the other hand, the entrainment rate across the TNTI varies with the ratio between the buoyancy and the flow shear strengths, represented by the Richardson number, Ri . This allows us to investigate how the properties of the TNTI vary to accommodate the entrainment variation with Ri and how these properties are

related to the VLCSs in the proximity of the TNTI.

The paper is organized as follows. Section 2 describes the experimental measurements, together with the TNTI identification and VLCSs eduction methods. Section 3 characterizes the VLCSs and analyzes their relationship with the TNTI and the entrainment process. The article closes with the discussion and conclusions in section 4.

2. Methods

2.1. Experiments

The gravity current data presented here were collected using the experimental apparatus developed in Krug *et al.* (2013). This setup is sketched in figure 1 and was designed to create a gravity current along the top of an inclined glass tank, which can be tilted between 0 and 90 degrees and whose dimensions are 2 m long and 0.5 m wide and high. The gravity current was realized by the continuous injection of a light fluid (a mixture of water and ethanol) along the top wall of the tank into a denser ambient fluid (a mixture of water and sodium chloride). As outlined in detail in Krug *et al.* (2014), a proper preparation of the solutions provides the desired density difference, while keeping the same refractive index in the two solutions. The latter is a crucial requirement for optical measurement techniques. During the experiment, the flow rate of the light fluid is driven by a water pump, measured via a flowmeter and its feedback is implemented as a closed loop control. In this way, a constant flow rate is guaranteed throughout the entire experiment. The natural transition to turbulence of the light fluid via Kelvin-Helmholtz instabilities requires an impracticably long tank (for a discussion, see Krug *et al.* 2013). It was therefore preferred to force the transition to turbulence at the inlet by means of a diffuser equipped with rotating flapping grids. In previous experimental studies by Krug *et al.* (2013) and Odier *et al.* (2014), it was shown that with this system the turbulence characteristics at a location sufficiently "far" from the inlet, as in the case of the present study, are independent on the inflow turbulence. The ambient entrained fluid was gently resupplied along the bottom of the tank to replenish entrained fluid. As noted by Krug *et al.* (2013) the particular value of the flow rate of the ambient fluid does not influence the entrainment rate, however a proper choice of it permits to avoid large-scale recirculation within the tank.

In this paper, we present results for three different flow cases. They differ in the initial density difference between the two solutions $\Delta\rho_0$ and the tank inclination α . An overview of the flow parameters is presented in Table 1. To compute the inflow Reynolds number, Re_0 , and the inflow Richardson number, Ri_0 , we used the inlet height d and the mean inflow velocity U_0 . Note that the label of the flow cases designates the respective value of Ri_0 . As shown by Ellison & Turner (1959), a gravity current adjusts itself to an equilibrium Ri number that depends only on the inclination of the tank α . Recently, Negretti *et al.* (2017) demonstrated that for a gravity current at the onset of the turbulence, the equilibrium Richardson number depends also on the inflow interfacial Richardson number. Maintaining a constant inflow velocity U_0 , we varied $\Delta\rho_0$ such that the flow results to be close to the equilibrium state near the inflow. This was guided by the numerical results of Krug *et al.* (2017b) and van Reeuwijk *et al.* (2019).

2.2. Measurements

Flow measurements were performed using three-dimensional particle tracking velocimetry (3D-PTV). In order to capture a large investigation volume while maintaining a fine spatial resolution, which is crucial for the VLCSs extraction method used here,

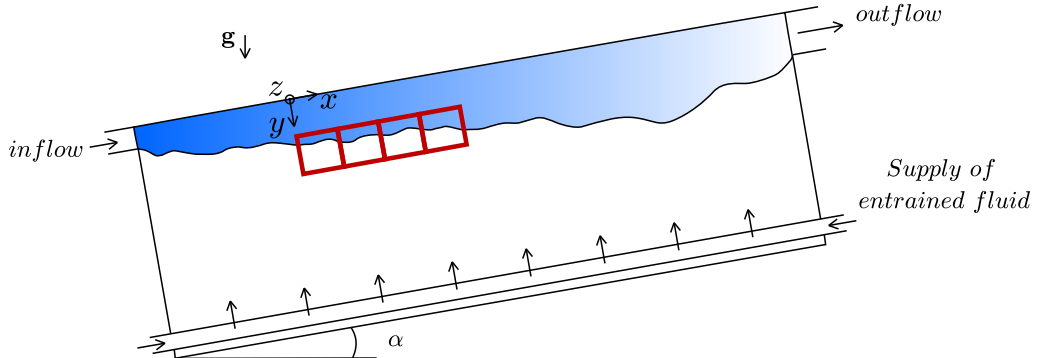


Figure 1: Sketch of the experimental setup. The blue area indicates the gravity current (lighter turbulent fluid) that flows along the top wall of the tank. At the bottom, heavy fluid is resupplied to make up for the entrained flux, while mixed fluid spills out of the tank through the outlet at the top-end of the tank. The four 3D-PTV investigation domains are indicated by red rectangles.

	Ri0	Ri10	Ri20
$U_0[cm/s]$	10	10	10
$\Delta\rho_0[g/l]$	0	2.1	4.1
$\alpha[^\circ]$	0	10	5
$d[cm]$	5	5	5
$Re_0 = U_0 d / \nu$	5000	5000	5000
$Ri_0 = g' d \sin \alpha / U_0^2$	0	0.10	0.20
$\eta[mm]$	0.23	0.29	0.31
$L[cm]$	1.00	0.96	1.00
$l_{sk}[cm]$	5.21	3.60	3.16
$u_\eta[cm/s]$	0.43	0.34	0.32
$Re_L = u' L / \nu$	152	107	102

Table 1: Overview of flow parameters for the three flow cases. The subscript 0 indicates the inflow parameters.

we performed measurements using four separate 3D-PTV systems. Their individual measurement domains were then stitched together in the streamwise direction. Each 3D-PTV system consisted of one high-speed camera, Mikrotron EoSens, equipped with a four-way image splitter to mimic a classical four-camera setup, which allowed a continuous recording of 120 s. The light source for illumination was a diode-pumped Nd-YLF laser (Quantronix, Darwin Duo 527 nm). As flow tracers, we used neutrally buoyant polyamide particles with a mean diameter of $100 \mu m$ (manufactured by *Evonik Industries*, Germany).

Each single 3D-PTV system covered an observation volume of about $9 cm \times 9 cm \times 4 cm$ in the x (streamwise), the y (wall-normal), and the z (spanwise) directions, respectively. The fields of view of the individual PTV systems overlapped for about $2 cm$ to track particles continuously across the different observation volumes. The start

of the measurement volume was located about 50 *cm* away from the inlet and covered roughly 31 *cm* in the streamwise direction (figure 2). For each observation volume, it was possible to track up to 3000 particles simultaneously. This corresponds to a mean inter-particle distance of about 3.5 *mm*, equivalent to roughly 10η , with $\eta = (\nu^3/\epsilon)^{1/4}$ being the Kolmogorov microscale, where ν is the kinematic viscosity and $\epsilon = u'^3/L$ is the local dissipation. Here, u' is the root mean square of the velocity fluctuation and L is the integral length scale of the turbulence, evaluated as the integral of the autocorrelation function of the streamwise velocity along x . The turbulence level was quantified through the integral Reynolds number $Re_L = u'L/\nu$ (Table 1). As can be observed, the stable stratification reduces the turbulence level. Reference length and time scales were evaluated at a height of about 7 *cm* from the top wall, a location that is far from the wall but still sufficiently far from the strongly intermittent region close to the TNTI. The spatial resolution achieved in our experiments is not sufficiently accurate to resolve the Kolmogorov scale. However, it was considered adequate for the purposes of the present work and a suitable compromise between a large enough spatial domain and spatial resolution. As shown by Krug *et al.* (2017*b*), the smallest convolutions of the TNTI are on the order of 10η and the TNTI geometry is therefore sufficiently captured by our measurements. The Lagrangian coherent structure extraction method explained below is based on vorticity. Given that the vorticity is somewhat under-resolved in our measurements, the extracted VLCSs represent those of a filtered velocity field, where we neglect the effect of Kolmogorov-sized eddies. The time resolution was set to 250Hz, which over-samples about 20 times τ_η , with $\tau_\eta = (\nu/\epsilon)^{1/2}$ being the Kolmogorov time scale. We applied a temporal Savitzky-Golay filter with a span of $0.5\tau_\eta$ to the velocity data. This reduced experimental noise due to position uncertainty of tracked tracer particles (Lüthi *et al.* 2005; Wolf *et al.* 2012).

A well-known feature of experimental particle tracking data is that particle trajectories have variable length and may be partly interrupted due to e.g. optical occlusions. However, the Lagrangian coherent structure extraction method explained below requires un-interrupted trajectories. We therefore interpolated the Lagrangian velocity data on an Eulerian grid with a spacing of 5η . Subsequently we advected fluid particles numerically from these Eulerian velocity fields. A similar procedure has been applied for example by Ouellette (2012). In figure 2, we show samples of numerically computed fluid trajectories. To estimate the error of numerically calculated fluid particle trajectories, we used the longest measured trajectories and computed the root mean square (r.m.s.) distance between particle positions at the end of the trajectories. For one full flow through time of the entire volume, we obtained an acceptable value of about one Kolmogorov length scale.

2.3. TNTI identification and local entrainment velocity

Following previous work, the identification of the TNTI was done using a threshold on the enstrophy field, $\omega^2 = \boldsymbol{\omega} \cdot \boldsymbol{\omega}$ where $\boldsymbol{\omega}$ is the vorticity vector (see e.g. Holzner *et al.* 2008; Krug *et al.* 2015). The TNTI location is then defined by an iso-surface corresponding to a specific ω_{th}^2 threshold. In the present investigation, the threshold was fixed at $\omega_{th}^2 = 2.5s^{-2}$ just above the noise level of the data. This value is very close to those chosen by Krug *et al.* (2015) for the same flow and by Wolf *et al.* (2012) for a turbulent jet. The local velocity propagation of the TNTI surface with respect to the fluid particles, the entrainment velocity v_n , was estimated using the direct approach, presented by Wolf *et al.* (2012). In their approach, v_n is computed from:

$$v_n = v_{\omega_{th}^2} - v_f, \quad (2.1)$$

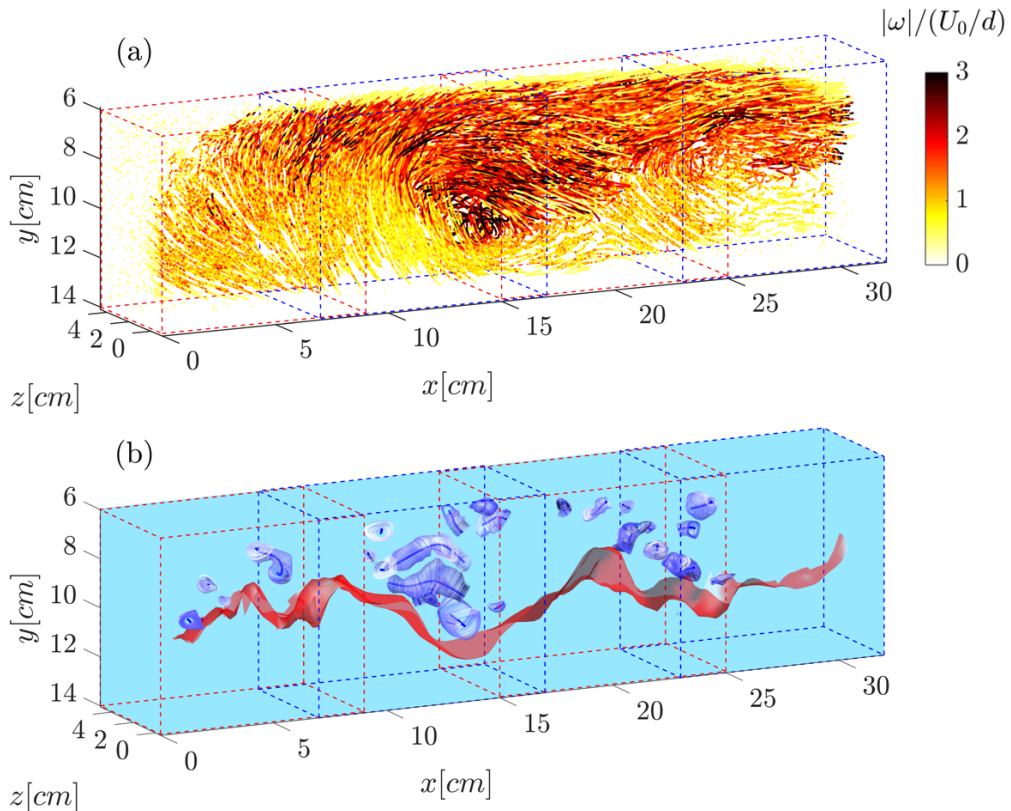


Figure 2: (a) Three-dimensional fluid trajectories color-coded with the norm of the vorticity for the flow case Ri_{20} . The time period shown here is equivalent to three turnover-times (defined in section 2.4) of the largest eddies. The four alternated red and blue rectangular outlines represent the four 3D-PTV observation volumes. (b) Corresponding three-dimensional VLCSs, represented by blue tubular surfaces (boundaries) surrounding one-dimensional curves (centers), and the TNTI of the gravity current (red open-surface). The region above the TNTI is turbulent, whereas below the flow is irrotational.

where $v_{\omega_{th}^2}$ is the local velocity of TNTI and v_f is the local flow velocity. To determine $v_{\omega_{th}^2}$, we used the positions of ω_{th}^2 -isosurface at consecutive time steps. Similar to the velocity data, we also applied a temporal filter to the measured TNTI interface locations to remove occasional spurious outliers in the irrotational region.

2.4. VLCSs education

The detection of the Lagrangian coherent vortices is based on LAVD theory. We recall the definition of LAVD:

$$LAVD_{t_0}^t(x_0) = \int_{t_0}^t |\omega(x(s; x_0), s) - \bar{\omega}(s)| ds. \quad (2.2)$$

where ω is the vorticity along fluid trajectories, $\bar{\omega}$ is its spatial average, and $x(t, x_0)$ denotes the fluid trajectory starting at x_0 at time t_0 . According to Haller *et al.* (2016), a rotational Lagrangian coherent vortex is defined as an evolving material domain filled

with a nested family of tubular surfaces of $LAVD_{t_0}^t(x_0)$ with outward decreasing LAVD values. The boundary of the VLCS is the outermost tubular level surface, whereas its center is the innermost member of the LAVD level-surface family. LAVD-based methods have been successfully applied in the past to 2D data of satellite oceanic velocity fields and DNS of forced turbulence, as well as to 3D data of the ocean model SOSE (Haller *et al.* 2016). Prior applications of the detection method to three-dimensional data utilized the physics and geometry of the problem to simplify the extraction of the structures. For example, the 3D vortex extracted by Haller *et al.* (2016) from the SOSE model, is a single vertically-oriented structure. In the present study, we implemented this method for multiple three-dimensional vortical structures extraction without a prior knowledge on the physics or geometry. Our algorithm can be described as a two-step procedure. In the first step, we compute one-dimensional curves representing the center of the structures and in a second step, we determine the boundaries of the VLCSs.

In Haller *et al.* (2016), the centers of VLCSs are defined by one-dimensional ridges of the LAVD field. In general, the computation of one-dimensional ridges in three dimensions is a challenging task. In the present work, we address this task by extending the 2D gradient climbing algorithm proposed by Mathur *et al.* (2007) to three-dimensions. This algorithm uses the property that trajectories computed on the gradient field of a scalar quantity tend to accumulate along the ridges of the scalar field. The final position of these trajectories can be exploited to determine one-dimensional candidates for the ridges identification. Our ridges extraction algorithm is implemented as follows:

(i) For any initial time t_0 , we determine narrow regions in the ridges neighborhood, where the magnitude of the $\nabla(LAVD)$ is higher than a pre-defined threshold and use points inside these regions as the initial conditions for computing numerically the solutions $\mathbf{x}_0(t)$ of the gradient dynamical system:

$$\frac{d\mathbf{x}_0}{dt} = \nabla LAVD_{t_0}^{t_0+T}(\mathbf{x}_0), \quad (2.3)$$

where t denotes the time and ∇ denotes the spatial gradient with respect to the initial position \mathbf{x}_0 . The solution $\mathbf{x}_0(t)$ takes the initial conditions to the closest ridge along the local gradient field of the LAVD.

(ii) For a given initial condition, the computation of the corresponding solution $\mathbf{x}_0(t)$ is stopped if the following two conditions hold: (a) the Hessian matrix $\nabla^2 LAVD_{t_0}^{t_0+T}(\mathbf{x}_0(t))$ has at least two negative eigenvalues (a prerequisite for a point to be on a ridge), and (b) the angle between the eigenvector $\mathbf{e}_{t_0}^{t_0+T}(\mathbf{x}_0(t))$ corresponding to the smaller-in-norm eigenvalue of the Hessian matrix $\nabla^2 LAVD_{t_0}^{t_0+T}(\mathbf{x}_0(t))$ and $\nabla LAVD_{t_0}^{t_0+T}(\mathbf{x}_0(t))$ shows no appreciable change (a sign of closeness to a nearby ridge). For large enough T , the eigenvector $\mathbf{e}_{t_0}^{t_0+T}(\mathbf{x}_0(t))$ will be approximately tangent to a ridge.

(iii) To determine the ridges candidates, we use the final positions of the solutions $\mathbf{x}_0(t)$ and select among them only points with a sufficiently close neighbor point. To this end, we use a pre-defined threshold on the distance between two points.

(iv) We then group together points belonging to the same ridge and order them. To order the points, we sort them in ascending order with respect to their x , y and z coordinates and select among the three sets, the one that minimizes the curve arc length.

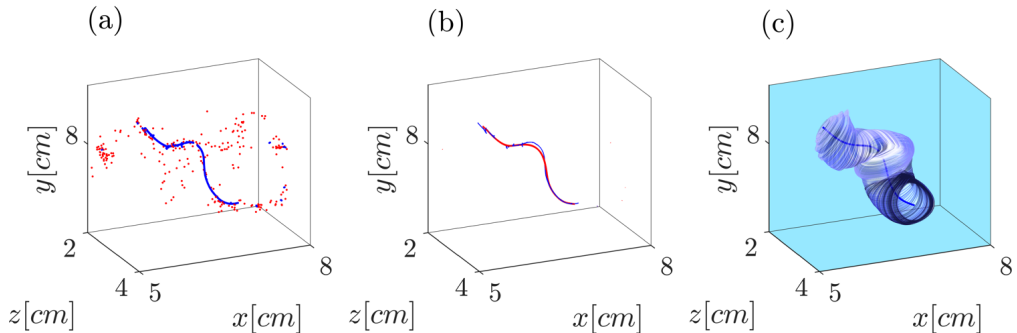


Figure 3: Example of VLCSSs extraction. In (a), the final position of the solution $\mathbf{x}_0(s)$ of equation 2.3 is shown. The blue dots are selected for the ridge construction, whereas the red ones are discarded. In (b), in blue, the connection of the points selected in (a) and its smooth fitting curve (red) are shown. The corresponding VLCSS is shown in (c).

(v) Finally, we smooth the ridges. By parametrizing their x , y and z coordinates with respect to the arc length, we fit them with a cubic smoothing spline.

In figure 3, we show an example of the application of the last three steps described above. In this case, part of the points in ridge proximity are not aligned along a 1D curve (figure 3(a)). We therefore select only points with sufficiently close neighbor points, sort them (blue curve in 3(b)) and apply a smoothing cubic spline (long blue curve in 3(c)). After computing the structures centers, we determined their boundaries using the following steps:

(i) For each point of a given ridge, we erect point-wise normal planes to the ridge curve and determine the in-plane outermost almost-convex LAVD contour that encircles the point. These curves are one-dimensional curves in 3D.

(ii) We then use these curves to build the VLCSSs boundaries. This is achieved for every pair of nearby curves by using the *MATLAB* function *convhull* to compute the lateral surface connecting them.

In figure 3(c), we show the result of the application of these steps to the ridges shown in figure 3(b). The second step of the construction of the boundaries of the VLCSS is slightly different from the one described in Haller *et al.* (2016) in that these authors use tubular level surfaces of a fixed LAVD value. We observed that tubular LAVD level surface typically enclosed only part of the LAVD ridges. That is, although perfectly aligned to the structures center and enclosed by almost-convex contours, part of the ridge remained outside of the structure (see the example in figure 4(a)), which is why we preferred to use the union of almost-convex contours. To give an impression on how the method performs on our data, we show several VLCSSs in figure 2(b). These are composed of tubular surfaces enclosing 1D-curves (centers), in the proximity of the TNTI, represented under the form of an open-surface. Here, the portion of the volume above the TNTI, where the VLCSSs are located, corresponds to the turbulent part, whereas the lower side corresponds to the irrotational flow. While some of the structures lie far from the TNTI, others are located close to it. The latter appear to shape the interface locally, as can be gleaned from the figure 4(c). This aspect will be investigated further in section 3.2.

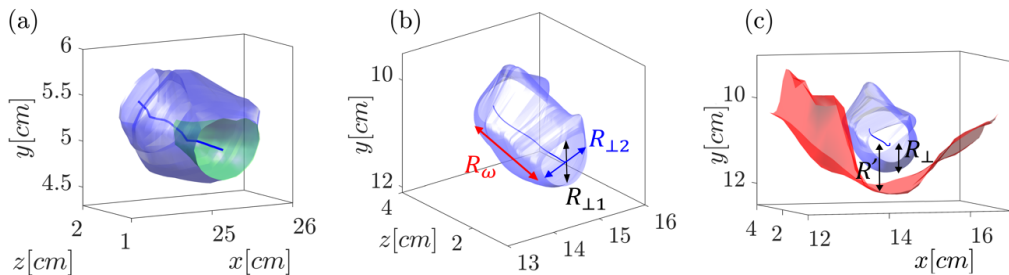


Figure 4: (a) VLCS reconstruction following the algorithm of Haller *et al.* (2016) (green inner-surface) and the modified algorithm introduced here (blue outer-surface). (b) Schematic of VLCSs dimensions. (c) Schematic representation of R_\perp , VLCSs (blue) cross-sectional size and R' , the distance between VLCSs center and the TNTI (red).

$\Delta t/t^*$	0	1	2	3	4
V_{VLCS}/L^3	0.28	0.41	0.41	0.37	0.39

Table 2: Average volume of the single VLCS, V_{VLCS} , for different extraction times of the flow case Ri20.

In the following, we discuss the effect of the extraction time Δt on the detected VLCSs, to explain how Δt was chosen for the present data. We remark that for short extraction times, in the limit of $\Delta t \rightarrow 0$, VLCSs tend to their Eulerian counter parts (see Haller 2015). In this case, the material coherence is guaranteed only instantaneously, in the sense that there is no certainty that an Eulerian structure remains coherent over any observation time $\Delta t > 0$. On the contrary, for very long extraction times, no-coherent structure can survive since the material coherence is limited in time for unsteady flows. For the vortical structures investigated here, the relevant temporal scale is the large eddy turnover time, which can be estimated as $t^* = L/u'$.

For the measurement setup adopted in this work, there is a natural upper limitation for Δt . This is related to the residence time of a fluid particle in the observation volume (i.e. the time spent by a particle inside the measurement volume). For the portion of the measurement volume closer to the wall, we observed that the residence time varies between one and four turnover times. In order to set the extraction time in formula (2.2), we tested different Δt values between zero (Eulerian proxy) and the maximum ($4t^*$) and investigated their effect in terms of V_{VLCS} , the average volume of a single VLCS. As can be observed in Table 2, V_{VLCS} is weakly influenced by the extraction time, at least in the range $t^* \leq \Delta t \leq 4t^*$. The same applies to other properties related to the size, the shape and the orientation of the VLCSs (not shown). The extraction time has a considerable impact on the number of the structures that can be extracted using our measurement setup. As Δt increases the number of trajectories entirely contained in the observation volume decreases drastically. This reduces the available volume for the VLCSs extraction and thus the number of the structures that can be deduced. As a consequence of this and observing that the extraction time appears to influence only weakly the characteristics of VLCSs, we opted to use $\Delta t = t^*$. We checked that qualitatively all results and conclusions remain the same for longer extraction times, albeit with reduced statistics.

2.5. VLCSs size and orientation

Given the three-dimensionality of VLCSs investigated here, we defined three characteristic dimensions (figure 4(b)): one along the VLCSs rotation axis and two in the cross-section. The two cross-sectional sizes are measured as follows. At each point of the center-line of the structure, we computed the point-wise perpendicular plane to the center-line. We then evaluated the intersection between this plane and the VLCS's boundary and we fitted an ellipse to the intersection points. By taking the average of the minor and major axes of the fitted ellipses, we assigned to each VLCS: $R_{\perp 1}$ (the minor-) and $R_{\perp 2}$ (the major cross-sectional size). The third dimension, R_{ω} , is given by the length of the axis of rotation. As can be observed in figure 2(b), some of the vortices are truncated in the rotation axis direction by the boundaries of the measurement domain. In such a case, we made an estimation of R_{ω} based on a quadratic fit. The fit was done in 1D using the average values between $R_{\perp 1}$ and $R_{\perp 2}$ along the rotation axis and using the zero crossing of the fitted curve. That is, we assumed that R_{ω} is finite and represented by the spatial distance between two cross-sections with zero area. The orientation of the VLCSs was assessed by computing the average unit vector \mathbf{n} tangent to the axis of rotation.

3. Results

3.1. VLCSs geometrical properties

The average size parameters of the VLCSs as a function of the initial Richardson number Ri_0 are presented in figure 5(a). Here, the three dimensions are normalized by the integral length scale of turbulence L , which is almost constant for all the flow cases (see Table 1). From figure 5(a), together with the observation that L is almost constant with Ri_0 , it follows that the mean dimensions of the VLCSs do not vary significantly with the stratification. The cross-sectional average sizes $R_{\perp 1}$ and $R_{\perp 2}$ are equal to approximately $0.6L$ and $0.95L$. This gives an idea of the shape of the cross section of the structures, which on average is an ellipse with eccentricity of roughly 0.6. The average size of the third dimension, the axis of rotation R_{ω} , is of order $7L$. If the two cross-sectional sizes are ordered as a consequence of their construction, the third dimension is technically free to vary, i.e. it can be smaller or larger than $R_{\perp 1}$ and $R_{\perp 2}$. However, it is evident from the figure 5(a) that the rotation axis of the VLCS is on average the longest one. The conclusion from this observation is that most of the structures appear to have a tubular shape. The inset in figure 5(a), in which we show the probability density functions (PDFs) of the three size parameters for Ri_{20} gives an impression about their distribution.

The VLCSs dimensions presented in figure 5(a) are measured at the initial time t_0 of their extraction. Solving the equation of motion between an initial time t_0 and a final time $t_0 + \delta t$ for the particles constituting the centers and the boundaries of the VLCSs, it is possible to advect the structures under the flow evolution and to evaluate their final size, and hence their growth rates, dR/dt . Here, δt was chosen to be equal to the extraction time. The growth rates of the cross-sectional sizes were evaluated computing $R_{\perp 1}$ and $R_{\perp 2}$ as described in the section 2.5 at the final time $t_0 + \delta t$. The growth rate of the axis of rotation was determined by the continuity equation, given that for a material structure $dR_{\perp 1}/dt + dR_{\perp 2}/dt + dR_{\omega}/dt = 0$. An alternative way to determine dR_{ω}/dt is to compute it by directly estimating R_{ω} as described in section 2.5 at t_0 respectively $t_0 + \delta t$. However, we preferred the use of the continuity equation in order to avoid the inaccuracies introduced by the estimation approach of R_{ω} when the structure is not

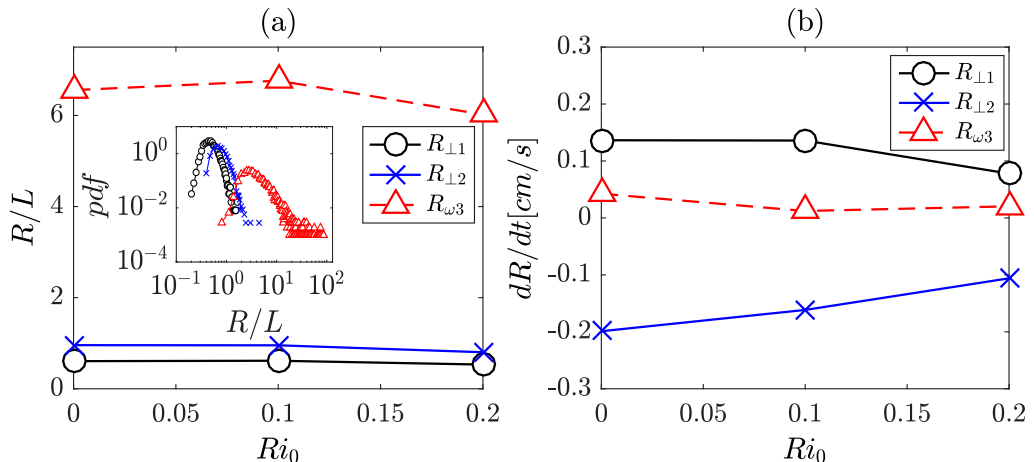


Figure 5: Average VLCSs dimensions (a) and their growth rates (b) as a function of the initial Richardson number Ri_0 .

fully contained in the observation volume. In figure 5(b), we display the average growth rates of the VLCS dimensions as a function of Ri_0 . The growth rates corresponding to the minor-axis and to the rotation axis are positive in sign, and thus these axes increase their sizes in time, whereas the growth rate of the major axis is negative. The positive growth of the rotation axis implies a predominant stretching of the vortical structures along the rotation axis. In general, the picture that emerges is that under the flow evolution the VLCSs are typically stretched and their cross-section tends towards a more isotropic shape compared to their initial conditions.

Further, figure 5(b) shows clearly that the growth rates diminish as Ri_0 increases. Thus, the stratification reduces the average VLCSs compression (of the intermediate axis) and stretching (of the smallest and the rotation axis dimensions). We also note that for all Ri_0 the magnitude of average growth rates is rather small and of the order of the Kolmogorov velocity scale magnitude u_η (see Table 1), meaning that the VLCSs are on average not very strongly stretched. This result confirms our expectations, since by definition VLCSs are materially coherent structures that are not supposed to undergo very significant deformation under flow evolution.

In figure 6, we present the orientation of the rotation axis of the VLCSs. Specifically, we plot the joint probability density functions (PDFs) of two components of the unit vector tangent to the axis of rotation of the VLCSs. Since there is no obvious choice in which direction the tangent vector should point, we show the absolute values of the two components.

For all the flow cases, the joint PDFs are biased towards values of $n_x \approx 1$. That is, the structures exhibit a preferential orientation in the streamwise direction. Similarly, there is a sizeable probability to observe VLCSs oriented along the spanwise direction ($n_z \approx 1$), whereas the probability of the wall-normal orientation ($n_x \approx n_z \approx 0$) is not significant. As the Richardson number increases, the spanwise orientation gains some more importance at the expense of the streamwise one (figure 6(c)).

To assess the shape of the structures, one can build a map of R_{max}/R_{min} and R_{int}/R_{min} , with R_{max} , R_{int} and R_{min} , representing respectively the major, the intermediate and the minor VLCSs size. We should mention here that $R_{\perp 1}$, $R_{\perp 2}$ and R_ω do not coincide respectively with R_{min} , R_{int} and R_{max} for all the structures, although we observed

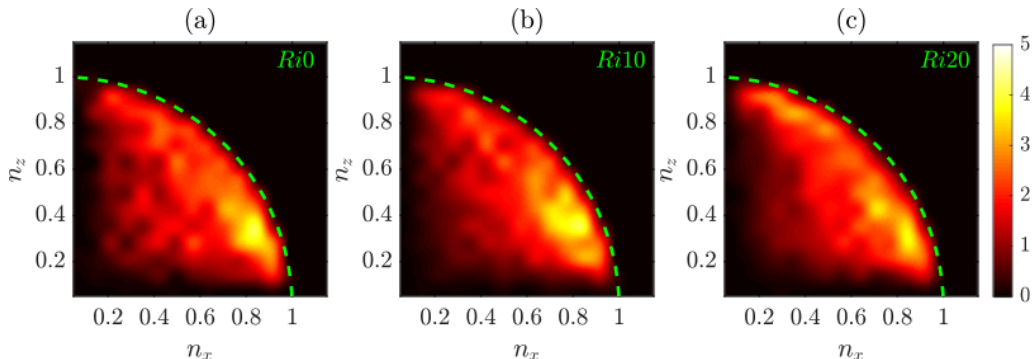


Figure 6: Joint PDFs of VLCSS orientation in the n_x - n_z plane at the initial time of the detection of the VLCSSs for Ri0 (left), Ri10 (center) and Ri20 (right). The wall-normal component n_y can be estimated from the joint PDFs reminding that $n_x^2 + n_y^2 + n_z^2 \approx 1$.

in figure 5 that this is true on average. The map is a useful tool to determine the shape of the VLCSSs. In particular, values of R_{max}/R_{min} and R_{int}/R_{min} close to the origin (1, 1) represent isotropic, sphere-like, structures. Values lying close to the abscissa denote tubular structures, whereas values in the proximity of bisector denote sheet-like structures. In figure 7, we show joint PDFs of the shape map. For all the flow cases, there is a clear prevalence of tubular structures, which persists with increasing stratification. The three joint PDFs show qualitatively similar behavior, with a peak of $(R_{max}/R_{min}, R_{int}/R_{min})$ between (3, 1) and (7, 1). The peak position is consistent with figure 5(a), in which we showed that the average value of the rotation axis R_ω is about seven times larger than $R_{\perp 1}$ and $R_{\perp 2}$.

3.2. Interaction between the TNTI and VLCSSs

In the following, we present the relationship between the TNTI and the nearby VLCSSs. Through conditional analysis, we provide evidence that the average interface height and the local entrainment velocity are locally modulated by the presence of VLCSSs. As observed in figure 2(b), part of the VLCSSs are located in the proximity of the TNTI. We selected VLCSSs that are sufficiently close to the TNTI by computing the ratio r between R' , the vertical distance of the center of the VLCS with respect to the TNTI, and R_\perp , the VLCSSs cross-sectional average radius, defined as the one half of the mean value between $R_{\perp 1}$ and $R_{\perp 2}$. A sample representation of R' and R_\perp can be found in figure 4(c). Given that in the non-turbulent region there is no vorticity, the VLCSSs cannot cross the TNTI. This implies that r cannot be smaller than one. For the following conditional analysis, we selected structures with r smaller than a threshold value $r_{th} = 2.5$, which was fixed after testing different values and observing qualitatively similar results.

In a second step, for each selected structure we resampled both, the instantaneous velocity field at the initial extraction time and the LAVD field around it, onto a uniform grid. For this operation, we positioned the frame of reference at the center of the VLCS and normalized the three dimensions x , y and z around the structure with the VLCSSs cross-sectional average radius R_\perp . The rationale was to have a common frame of reference for all VLCSSs and to compare flow fields, around VLCSSs of the same normalized size. Taking the average of the LAVD fields around the VLCSSs, we extracted a mean representative VLCS, that is, we applied the extraction algorithm described in 2.4 to the average LAVD field.

Applying the same coordinate transformation to the TNTI surfaces in the proximity

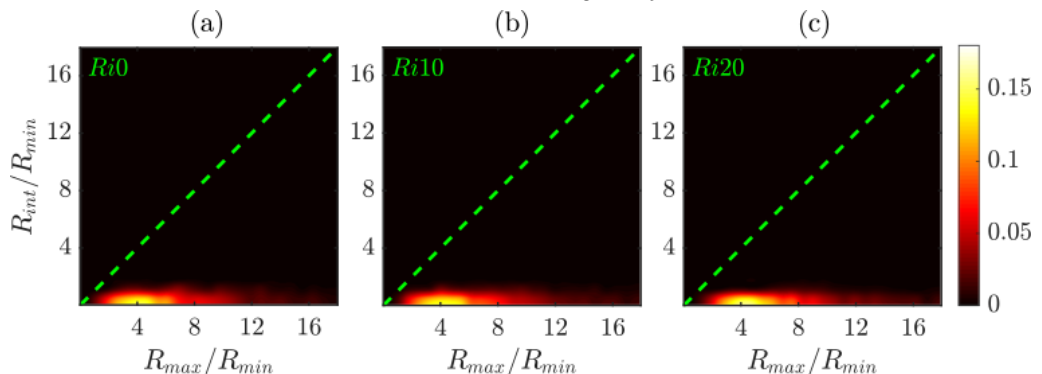


Figure 7: Joint PDFs of VLCSs shape in the R_{max}/R_{min} and R_{int}/R_{min} map at the initial time of the detection of the VLCSs for $Ri0$ (left), $Ri10$ (center) and $Ri20$ (right).

of the VLCSs, we computed the conditional average height of the TNTI. Moreover, at each location of the average height, we evaluated a mean local entrainment velocity $\langle v_n \rangle$. To this end, we computed the mean of instantaneous entrainment velocities near the structures. It is worth mentioning here that the high variance of the TNTI for the unstratified case $Ri0$ did not permit us to include this flow case in our analysis, given that the TNTI is observable in the measurement domain for a limited amount of instances, which did not allow us to obtain a meaningful statistical analysis.

In figure 8, we present the results for $Ri10$ and $Ri20$. The centers of the structures are represented by the continuous lines close to the origin of the frame of reference and their boundaries by tubular surfaces enclosing them. Below the structures, the open surfaces represent the average TNTI positions, which we color-coded with the average local entrainment velocity. Around each structure, we show the direction of the average flow fields with cones that point along the velocity vector with the size representing its magnitude.

The first observation that emerges from the figure 8 is that the average VLCS is oriented differently for the two flow cases. For $Ri10$, the average VLCS is orientated in the streamwise direction (figure 8(a)), whereas for $Ri20$, the VLCS is mainly oriented in the spanwise direction (figure 8(d)). In both flow cases, the TNTI is positioned at about $y/R \approx -2$ and the surface is clearly modulated by the nearby structure, having a curvature that follows that of the VLCSs boundaries. As the stratification increases, the curvature of the TNTI is observed to reduce, which is consistent with a decrease of the mean surface area of the TNTI.

In order to reveal the effect of the orientation of the VLCSs on the shape of the TNTI, we conditioned our analysis to streamwise (figure 8(b) and (e)), respectively spanwise oriented structures. To this end, we compared n_x and n_z , evaluated as described in section 2.5. For a given VLCS, if $n_x > n_z$, the structure is considered to be oriented approximately in the streamwise direction, otherwise it is considered to be oriented in the spanwise direction. From the second and the third column of the figure 8, it appears clearly that the interface shape recalls that of the VLCSs boundaries having a larger curvature in the plane orthogonal to the rotation axis of the VLCS. Consider for example figure 8(e), in which we conditioned our analysis to VLCSs of $Ri20$ oriented in the streamwise direction. The curvature of the average TNTI is almost entirely contained in $y-z$ planes, which are orthogonal to the center of the structure, while they are almost flat in the $x-y$ planes. Similarly, the curvature of the TNTI near the structures oriented

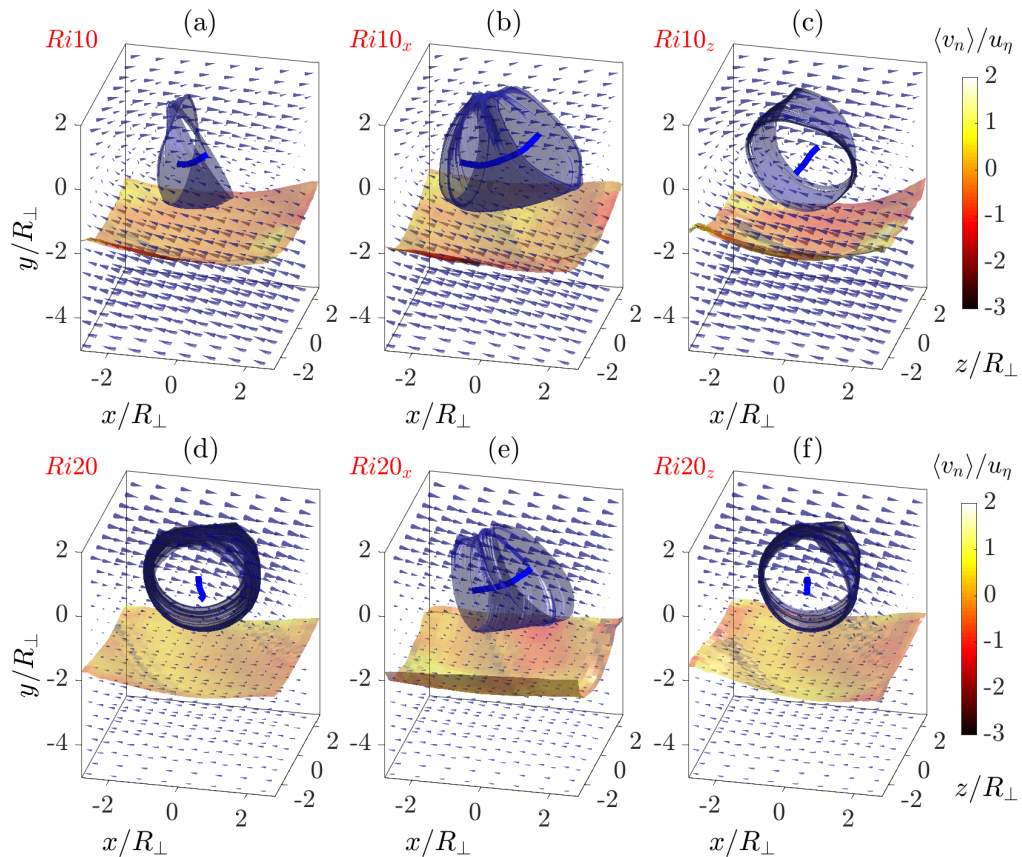


Figure 8: Conditional average VLCS and TNTI position for Ri10 (upper-row) and Ri20 (lower-row). VLCSs centers are represented by the continuous blue lines and their boundaries by the tubular surfaces. The open surface is the conditioned TNTI mean position, color-coded with the average of the local entrainment velocity. The direction and the size of the vectors represent the conditional average velocity field. In the first column ((a) and (d)) the conditional analysis is made for all the structures, whereas in second ((b) and (e)) and the third column ((c) and (f)) the analysis is conditioned also on the orientation of the structures. The structures are oriented prevalently in the streamwise direction in (b) and (e), respectively in the spanwise direction in (c) and (f).

prevalently in the spanwise direction is mostly limited to $x - z$ planes (see for example figure 8(c)). The average entrainment velocity $\langle v_n \rangle$ is shown in color on the TNTI surface. As it is common practice, we normalized v_n with the Kolmogorov velocity microscale u_η . Here, negative values of v_n represent entrainment of dense irrotational fluid from below into the lighter turbulent fluid. The spatial distribution of $\langle v_n \rangle / u_\eta$ on the TNTI shows a similar pattern for the two flow cases in figure 8, with higher negative values downstream with respect to the center of the structure, that is to say, close to $x/R_\perp \approx 2$ for the VLCSs oriented in the spanwise direction. For the structures oriented in the streamwise direction, $\langle v_n \rangle / u_\eta$ has higher negative values at the sides of the VLCSs near $z/R_\perp \approx \pm 2$. In correspondence of the center of the VLCS, for $(x/R_\perp, y/R_\perp) \approx (0, 0)$ higher or even positive values of $\langle v_n \rangle / u_\eta$ are observed (see e.g. figure 8(d)). The maximum negative value of $\langle v_n \rangle / u_\eta$ is different between the two flow conditions, diminishing (in terms of

	<i>Ri</i> 10	<i>Ri</i> 20
R_H/R_\perp	6.6	9.4
$\langle v_n \rangle / u_\eta$	-0.27	-0.03

Table 3: Average entrainment velocity and mean curvature of the surface of TNTI conditioned on the presence of VLCSs for *Ri*10(a) and *Ri*20(b).

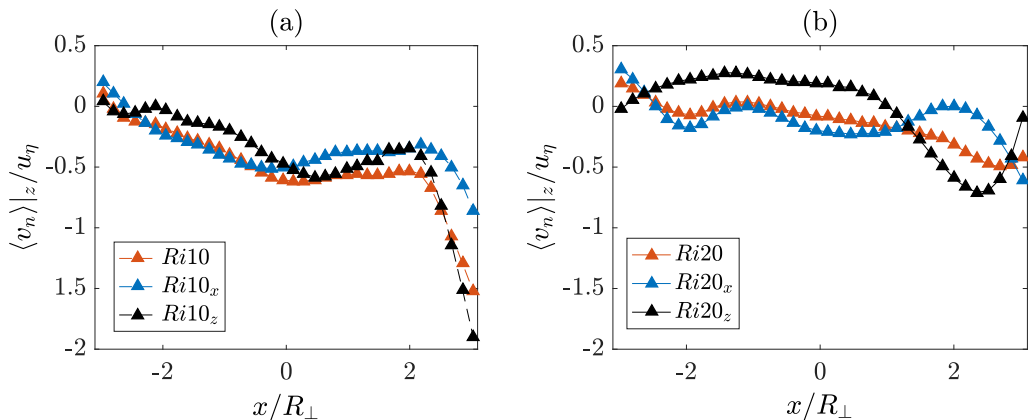


Figure 9: Conditioned spanwise average of the local entrainment velocity in the proximity of the VLCSs related to the figures 8(a) and (d).

absolute value) for increasing stratification, from $\langle v_n \rangle / u_\eta \approx -1$ for *Ri*10 (figure 8(a)) to $\langle v_n \rangle / u_\eta \approx -0.5$ of *Ri*20 (figure 8(b)). As previously observed, just below the center of the VLCSs, positive values of $\langle v_n \rangle / u_\eta$ can be noticed. The existence of regions of positive $\langle v_n \rangle / u_\eta$ (detrainment) is well known. Wolf *et al.* (2012) showed that v_n / u_η can be positive in regions with positive curvature of the TNTI (concave curvature looking to the interface from the turbulent side). As seen in figure 2, some of these bulges host VLCSs. As shown by others (e.g. Watanabe *et al.* 2014; Krug *et al.* 2017a), unconditioned averages of the $\langle v_n \rangle / u_\eta$ are negative (entrainment), but instantaneous positive (detrainment) values can be observed (Mistry *et al.* 2019). To interpret the latter, one can take into account the local entrainment velocity decomposition based on the turbulent enstrophy equation introduced by Holzner & Lüthi (2011). Based on their decomposition, $\langle v_n \rangle / u_\eta$ can be locally positive if the enstrophy destruction outweighs both the enstrophy production, which is comparatively small in viscous superlayer, and the viscous diffusion, which is mostly positive in the viscous superlayer. This can lead to the reduction of the local enstrophy level below the threshold used for the TNTI identification.

In Table 3, we present the mean radius of curvature R_H of the TNTI surfaces shown in figure 8(a) and (d). The mean radius of curvature increases from $R_H/R_\perp = 6.6$ for *Ri*10 to $R_H/R_\perp = 9.4$ for *Ri*20. The effectiveness of the VLCSs to contort the average interface reduces with increasing stratification. Although the mean radius of curvature is not a direct measure of the surface area of TNTI, it is clear that at higher values of R_H correspond lower values of the surface area. It follows thus that the conditioned surface area of the TNTI decreases with increasing stratification, which is consistent with earlier work (see e.g. Krug *et al.* 2015). Furthermore, in Table 3, we report $\langle v_n \rangle / u_\eta$ the

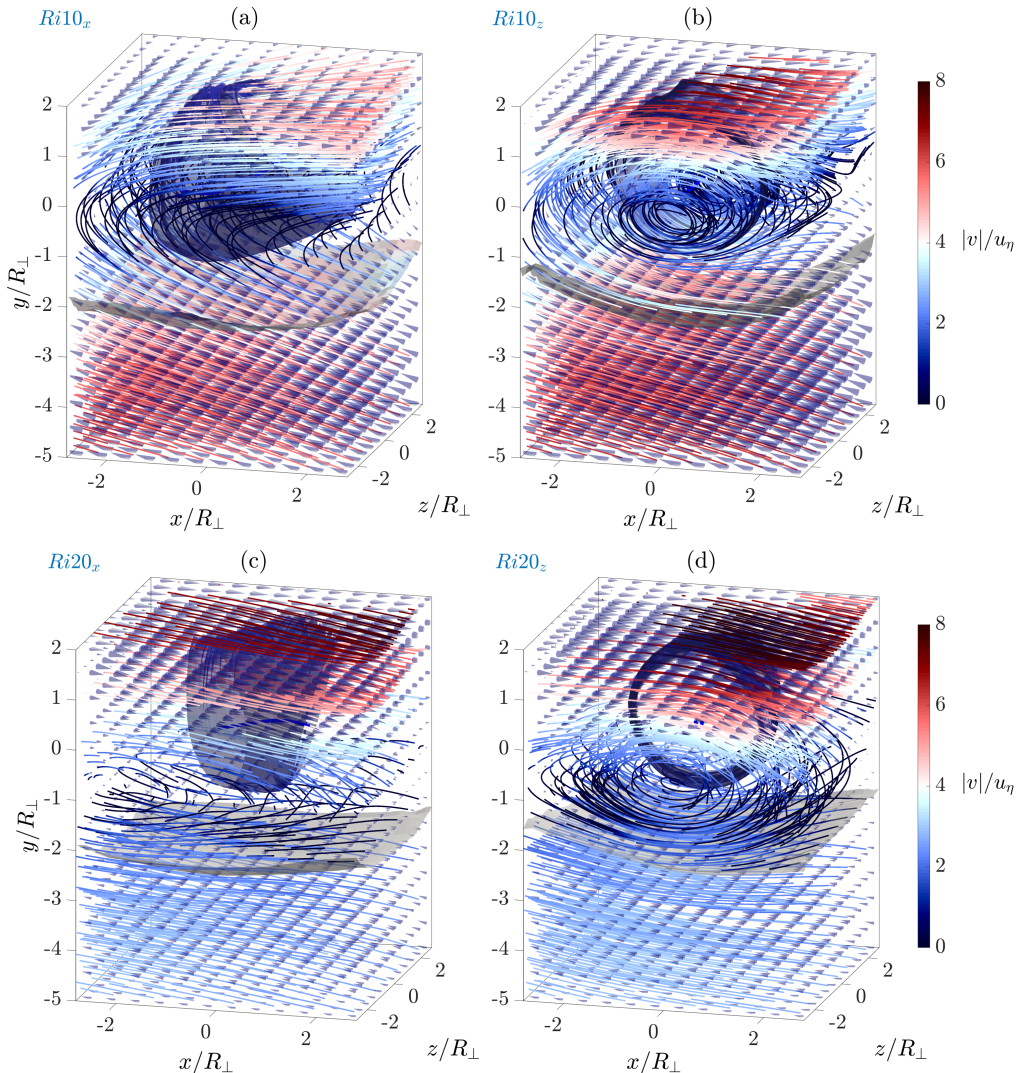


Figure 10: Flow visualization. Streamlines of figure 8, color-coded with the average velocity magnitude.

average of the local entrainment velocity over the TNTI surfaces in figures 8(a) and (d). The average of $\langle v_n \rangle / u_\eta$ exhibit a higher value for the lower stratification passing from $\langle v_n \rangle / u_\eta = -0.27$ for Ri10 to $\langle v_n \rangle / u_\eta = -0.03$ for Ri20.

In order to further illustrate how the large-scale VLCSs influence the small scale entrainment, in figure 9 we show the the spanwise average of $\langle v_n \rangle / u_\eta$ corresponding figures 8(a) and (d). In both cases shown in figure 9, the entrainment velocity is higher in the downstream region ($x/R_\perp \approx 2$), and lower or even positive (figure 9(b)) in the proximity of the center of the VLCS ($x/R_\perp \approx 0$). In a similar fashion to the figure 8, we show the effect of the orientation of the structures on the entrainment velocity. For Ri10 (figure 9(a)), it is clear that the entrainment has the same behavior for both, the structures oriented in the spanwise and in the streamwise directions. For Ri20 (figure 9(b)), $\langle v_n \rangle / u_\eta$ has considerably smaller negative values and for the structures oriented

in the spanwise direction, it has positive values around 0.2 for $x/R_{\perp} \approx 0$.

Finally, we analyze how VLCs near the TNTI influence the flow around them. The impact of the VLCs on the mean flow in proximity of the TNTI surface results different for the two flow conditions shown in the figure 8. For Ri10, no clear influence of the VLCs can be observed (figure 8(a)). However, the spanwise oriented structures (figure 8(c)) organize the flow both, inside and outside the turbulent zone. Inside the turbulent region, the average flow field results to revolve around the center of the structure, giving rise to a rotational motion, whereas outside, it is deviated towards the upstream region. In the case of Ri20, this behavior can be observed without the need of conditioning on the orientation of the VLCs (figure 8(d)). However, this flow pattern is reinforced when only spanwise oriented structures are considered (figure 8(f)).

For a clearer visualization, we display in figure 10 the streamlines of the average flow fields around the conditionally oriented structures shown in figure 8. Here, the streamlines are color-coded with the local velocity magnitude and the TNTI is represented by the gray-transparent open surface, positioned below the VLCS. For the structures oriented in the streamwise direction (figure 10(a) and (c)), the streamlines in the non-turbulent zone appear to be rather horizontal, curving in the proximity of the VLCS ($y/R_{\perp} \approx 0$) and following the direction of the mean flow in the turbulent region. In both cases, the magnitude of the velocity field is higher far from the TNTI, both on the non-turbulent and the turbulent regions. When the spanwise oriented structures are considered (figure 10(b) and (d)), a different flow organization arises. Outside the turbulent zone, far from the TNTI, the streamlines are again almost horizontal, similar to those close to the streamwise oriented structures in figure 10(a) and (c). However, in the turbulent side, they follow the rotational motion induced by the VLCs, curling up around the structures. This is evident in the figures 10(c) and (d), where the swirling motion due to the presence of the structures can be clearly distinguished. For Ri20 (figure 10(d)), the streamlines follow almost tangentially the TNTI. The velocities along the streamlines forming the swirling motion inside the turbulent zone are higher for both Ri10 and Ri20 on the upper side of the structures ($y/R_{\perp} \approx \pm 1$), decreasing in the proximity of the center of the structures and increasing again in the non-turbulent side.

4. Discussion and summary

In this paper, we focused on the detection and characterization of Lagrangian vortical coherent structures (VLCs) and their influence on the turbulent/non-turbulent interface (TNTI) and entrainment of a gravity current. Using 3D-PTV data, the VLCs were educed by means of the so-called Lagrangian-Averaged Vorticity Deviation (LAVD) method. The TNTI was identified using an enstrophy threshold, whereas its entrainment velocity was computed through a direct method described in Wolf *et al.* (2012).

In the section 3.1, we described the geometrical characteristics of the VLCs. In particular, in figure 5(a) we observed that the average cross-sectional dimensions of the VLCs are of order of the integral length scale of the turbulence L . By normalizing them with L , almost no-variation of their size with increasing stratification was noticed. Thus, the size of the VLCs appeared to scale with integral length scale. A similar observation was made for the largest vortical structures near the TNTI of a turbulent jet by da Silva & dos Reis (2011). Using a low-pressure iso-surface for the structures eduction, the authors found that the radius of what they call large-scale vortical structures is of order of Taylor microscale. Furthermore, analyzing the growth rates of the dimensions of the VLCs, we noticed that VLCs are predominantly stretched and in time, their cross-sections tend towards a rather isotropic shape. This is reminiscent of the predominant

vortex stretching mechanism (Tsinober 2000), which is well known e.g. since the initial studies by Chong *et al.* (1990), Cantwell (1993) and Soria *et al.* (1997) on the invariants of velocity gradient tensor. Through coarse grained and filtered velocity gradient tensors, Meneveau (2011) demonstrated that predominant stretching is discernible also at larger flow scales that are well in the inertial range, as is it the case for the ones investigated here.

In figure 6 and 7, we showed that on average the VLCSs are of tubular-shape orientated mainly in the streamwise direction. The fact that the structures are prevalently oriented in the streamwise direction is interesting, given that in our flow, the mean vorticity is oriented in the spanwise direction. A well known picture in wall-bounded turbulence is that an initially spanwise oriented vortex, formed near the wall of the boundary layer, is disturbed by an ejection event that rises part of the vortex tube at height where the mean flow is faster. The mean flow advects this coherent mass faster than the vortex tube near the wall tilting its legs towards vertical planes, in which they are stretched by the mean shear (Kim & Adrian 1999). We speculate that a similar mechanism may be at the base of formation of the VLCSs investigate here. In the mixing layer of the gravity current, initial vortices form via a Kelvin-Helmholtz type mechanism and are then tilted by turbulence and the mean shear. In figure 6, we also noted that as the stratification increases, more structures tend to be oriented in spanwise direction. We associate this to the mechanism described before. Indeed, as the stratification increases the vertical motion of the fluid is known to be reduced. This attenuates sweeps and ejections, with the consequence that the probability to observe spanwise oriented structures may be higher. Moreover, the orientation of the structures close to the TNTI was shown to be almost horizontal. This is a consequence of the fact that the VLCSs cannot cross the interface and cannot finish or start on it. This is in line with the findings of da Silva & dos Reis (2011) in the case of a planar turbulent jet.

In subsection 3.2, we investigated the interaction between large scale VLCSs and the TNTI, with a focus on both elements constituting the entrainment process, namely, the TNTI area and the local entrainment velocity. We showed that the VLCSs modulate the TNTI height, thereby increasing the TNTI surface area. A similar observation was done by Lee *et al.* (2017) for the TNTI height of a TBL. Here the authors conducted a conditional analysis based on LSMs position, showing that the interface is locally contorted by the LSMs. In both examples, the gravity current and the TNL, it is demonstrated that the large-scale flow structures enhance the TNTI area thereby augmenting the entrainment flux. Moreover, we showed that the local entrainment velocity at the smaller scales of the turbulence is modulated by the large scale VLCSs (figure 8). In particular, the local entrainment velocity was seen to be higher downstream with respect to the position of the VLCSs, decreasing and becoming even positive (detrainment) just beneath the center of the structure. We hypothesize that this might be connected to presence of the VLCS, which induces a motion tangent to the surface of the TNTI locally reducing the entrainment rate. The visualization of streamlines of the mean velocity field supports this idea. A similar remark was made by Bisset *et al.* (2002) for the instantaneous streamlines near a bulge of the TNTI of a turbulent wake. Here the authors observed that the streamlines enter it the turbulent side (high entrainment) only in regions with a convex curvature of the surface as seen from the turbulent side (see figure 15 in Bisset *et al.* 2002), whereas beneath the bulge the streamlines are almost horizontal (low entrainment or detrainment). In figure 2, we observed that part of these bulges hosts a VLCS, which is compatible with findings in Bisset *et al.* (2002). A more recent work by Mistry *et al.* (2019), which discusses the existence of instantaneous detrainment zones in a turbulent jet, further supports our

observations on the detrainment near the VLCSs. Here, the authors show that similarly to our findings high detrainment is observed when the fluid moves tangentially to the interface on both the sides of the TNTI.

We are grateful for financial support from DFG priority program SPP 1881 under grant number HA 7497/1-1.

REFERENCES

- BISSET, D. K., HUNT, J. C. R. & ROGERS, M. M. 2002 The turbulent/non-turbulent interface bounding a far wake. *J. Fluid Mech.* **451**, 383–410.
- CANTWELL, B. J. 1993 On the behavior of velocity gradient tensor invariants in direct numerical simulations of turbulence. *Phys. Fluids A* **5** (8), 2008–2013.
- CHONG, M. S., PERRY, A. E. & CANTWELL, B. J. 1990 A general classification of three-dimensional flow fields. *Phys. Fluids A* **2** (5), 765–777.
- CORRSIN, S. & KISTLER, A. L. 1955 Free-stream boundaries of turbulent flows .
- DIMOTAKIS, P. E. 2000 The mixing transition in turbulent flows. *J. Fluid Mech.* **409**, 69–98.
- ELLISON, T. H. & TURNER, J. S. 1959 Turbulent entrainment in stratified flows. *J. Fluid Mech.* **6** (3), 423–448.
- HADJIGHASEM, A. & HALLER, G. 2016 Geodesic transport barriers in jupiter’s atmosphere: A video-based analysis. *SIAM Rev.* **58** (1), 69–89.
- HALLER, G. 2015 Lagrangian coherent structures. *Annu. Rev. Fluid Mech.* **47**, 137–162.
- HALLER, G. 2016 Dynamic rotation and stretch tensors from a dynamic polar decomposition. *J. Mech. Phys. Solids* **86**, 70–93.
- HALLER, G. & BERON-VERA, F. J. 2013 Coherent lagrangian vortices: The black holes of turbulence. *J. Fluid Mech.* **731**.
- HALLER, G., HADJIGHASEM, A., FARAZMAND, M. & HUHN, F. 2016 Defining coherent vortices objectively from the vorticity. *J. Fluid Mech.* **795**, 136–173.
- HALLER, G. & YUAN, G. 2000 Lagrangian coherent structures and mixing in two-dimensional turbulence. *Physica D* **147** (3-4), 352–370.
- HOLZNER, M., LIBERZON, A., NIKITIN, N., LÜTHI, B., KINZELBACH, W. & TSINOBER, A. 2008 A lagrangian investigation of the small-scale features of turbulent entrainment through particle tracking and direct numerical simulation. *J. Fluid Mech.* **598**, 465–475.
- HOLZNER, M. & LÜTHI, B. 2011 Laminar superlayer at the turbulence boundary. *Phys. Rev. Lett.* **106** (13), 134503.
- HUNT, J. C. R., WRAY, A. A. & MOIN, P. 1988 Eddies, streams, and convergence zones in turbulent flows .
- JEONG, J. & HUSSAIN, F. 1995 On the identification of a vortex. *J. Fluid Mech.* **285**, 69–94.
- KIM, K. C. & ADRIAN, R. J. 1999 Very large-scale motion in the outer layer. *Phys. Fluids* **11** (2), 417–422.
- KRUG, D., CHUNG, D., PHILIP, J. & MARUSIC, I. 2017a Global and local aspects of entrainment in temporal plumes. *J. Fluid Mech.* **812**, 222–250.
- KRUG, D., HOLZNER, M., LÜTHI, B., WOLF, M., KINZELBACH, W. & TSINOBER, A. 2013 Experimental study of entrainment and interface dynamics in a gravity current. *Exp. Fluids* **54** (5), 1530.
- KRUG, D., HOLZNER, M., LÜTHI, B., WOLF, M., KINZELBACH, W. & TSINOBER, A. 2015 The turbulent/non-turbulent interface in an inclined dense gravity current. *J. Fluid Mech.* **765**, 303–324.
- KRUG, D., HOLZNER, M., LÜTHI, B., WOLF, M., TSINOBER, A. & KINZELBACH, W. 2014 A combined scanning ptv/lif technique to simultaneously measure the full velocity gradient tensor and the 3d density field. *Meas. Sci. Technol.* **25** (6), 065301.
- KRUG, D., HOLZNER, M., MARUSIC, I. & VAN REEUWIJK, M. 2017b Fractal scaling of the turbulence interface in gravity currents. *J. Fluid Mech.* **820**.
- LEE, J., SUNG, H. J. & ZAKI, T. A. 2017 Signature of large-scale motions on turbulent/non-turbulent interface in boundary layers. *J. Fluid Mech.* **819**, 165–187.

- LÜTHI, B., TSINOBER, A. & KINZELBACH, W. 2005 Lagrangian measurement of vorticity dynamics in turbulent flow. *J. Fluid Mech.* **528**, 87–118.
- MATHEW, J. & BASU, A. J. 2002 Some characteristics of entrainment at a cylindrical turbulence boundary. *Phys. Fluids* **14** (7), 2065–2072.
- MATHUR, M., HALLER, G., PEACOCK, T., RUPPERT-FELSOT, J. E. & SWINNEY, H. L. 2007 Uncovering the lagrangian skeleton of turbulence. *Phys. Rev. Lett.* **98** (14), 144502.
- MENEVEAU, C. 2011 Lagrangian dynamics and models of the velocity gradient tensor in turbulent flows. *Annu. Rev. Fluid Mech.* **43**, 219–245.
- MISTRY, D., PHILIP, J. & DAWSON, J. R. 2019 Kinematics of local entrainment and detrainment in a turbulent jet. *J. Fluid Mech.* **871**, 896–924.
- NEGRETTI, M. E., FLÒR, J. B. & HOPFINGER, E. J. 2017 Development of gravity currents on rapidly changing slopes. *J. Fluid Mech.* **833**, 70–97.
- ODIER, P., CHEN, J. & ECKE, R. E. 2014 Entrainment and mixing in a laboratory model of oceanic overflow. *J. Fluid Mech.* **746**, 498–535.
- OUELLETTE, N. T. 2012 On the dynamical role of coherent structures in turbulence. *C. R. Phys.* **13**, 866–877.
- VAN REEUWIJK, M., HOLZNER, M. & CAULFIELD, C. P. 2019 Mixing and entrainment are suppressed in inclined gravity currents. *J. Fluid Mech.* **873**, 786–815.
- DA SILVA, C. B., HUNT, J. C. R., EAMES, I. & WESTERWEEL, J. 2014 Interfacial layers between regions of different turbulence intensity. *Annu. Rev. Fluid Mech.* **46**, 567–590.
- DA SILVA, C. B. & DOS REIS, R. J. N. 2011 The role of coherent vortices near the turbulent/non-turbulent interface in a planar jet. *Phil. Trans. R. Soc. A* **369** (1937), 738–753.
- SILVA, T. S., ZECCHETTO, M. & DA SILVA, C. B. 2018 The scaling of the turbulent/non-turbulent interface at high reynolds numbers. *J. Fluid Mech.* **843**, 156–179.
- SORIA, J., OOI, A. & CHONG, M. S. 1997 Volume integrals of the qa-ra invariants of the velocity gradient tensor in incompressible flows. *Fluid Dyn. Res.* **19** (4), 219–233.
- SREENIVASAN, K. R., RAMSHANKAR, R. & MENEVEAU, C. H. 1989 Mixing, entrainment and fractal dimensions of surfaces in turbulent flows. *Proc. R. Soc. Lond. A* **421** (1860), 79–108.
- TOWNSEND, A. A. R. 1980 *The structure of turbulent shear flow*. Cambridge university press.
- TRITTON, D. J. 1988 *Physical fluid dynamics*, Clarendon.
- TSINOBER, A. 2000 *Vortex stretching versus production of strain/dissipation. Turbulence Structure and Vortex Dynamics* pp. 164–191.
- TSINOBER, A. 2009 An informal conceptual introduction to turbulence, , vol. 483. Springer.
- WATANABE, T., SAKAI, Y., NAGATA, K., ITO, Y. & HAYASE, T. 2014 *Enstrophy and passive scalar transport near the turbulent/non-turbulent interface in a turbulent planar jet flow. Phys. Fluids* **26** (10), 105103.
- WESTERWEEL, J., FUKUSHIMA, C., PEDERSEN, J. M. & HUNT, J. C. R. 2005 *Mechanics of the turbulent-nonturbulent interface of a jet. Phys. Rev. Lett.* **95** (17), 174501.
- WESTERWEEL, J., FUKUSHIMA, C., PEDERSEN, J. M. & HUNT, J. C. R. 2009 *Momentum and scalar transport at the turbulent/non-turbulent interface of a jet. J. Fluid Mech.* **631**, 199–230.
- WOLF, M., LÜTHI, B., HOLZNER, M., KRUG, D., KINZELBACH, W. & TSINOBER, A. 2012 *Investigations on the local entrainment velocity in a turbulent jet. Phys. Fluids* **24** (10), 105110.